

Computerized Detection of Lung Nodules by Means of “Virtual Dual-Energy” Radiography

Sheng Chen* and Kenji Suzuki, *Member, IEEE*

Abstract—Major challenges in current computer-aided detection (CADe) schemes for nodule detection in chest radiographs (CXR) are to detect nodules that overlap with ribs and/or clavicles and to reduce the frequent false positives (FPs) caused by ribs. Detection of such nodules by a CADe scheme is very important, because radiologists are likely to miss such subtle nodules. Our purpose in this study was to develop a CADe scheme with improved sensitivity and specificity by use of “virtual dual-energy” (VDE) CXRs where ribs and clavicles are suppressed with massive-training artificial neural networks (MTANNs). To reduce rib-induced FPs and detect nodules overlapping with ribs, we incorporated the VDE technology in our CADe scheme. The VDE technology suppressed rib and clavicle opacities in CXRs while maintaining soft-tissue opacity by use of the MTANN technique that had been trained with real dual-energy imaging. Our scheme detected nodule candidates on VDE images by use of a morphologic filtering technique. Sixty morphologic and gray-level-based features were extracted from each candidate from both original and VDE CXRs. A nonlinear support vector classifier was employed for classification of the nodule candidates. A publicly available database containing 140 nodules in 140 CXRs and 93 normal CXRs was used for testing our CADe scheme. All nodules were confirmed by computed tomography examinations, and the average size of the nodules was 17.8 mm. Thirty percent (42/140) of the nodules were rated “extremely subtle” or “very subtle” by a radiologist. The original scheme without VDE technology achieved a sensitivity of 78.6% (110/140) with 5 (1165/233) FPs per image. By use of the VDE technology, more nodules overlapping with ribs or clavicles were detected and the sensitivity was improved substantially to 85.0% (119/140) at the same FP rate in a leave-one-out cross-validation test, whereas the FP rate was reduced to 2.5 (583/233) per image at the same sensitivity level as the original CADe scheme obtained (Difference between the specificities of the original and the VDE-based CADe schemes was statistically significant). In particular, the sensitivity of our VDE-based CADe scheme for subtle nodules (66.7% = 28/42) was statistically significantly higher than that of the original CADe scheme (57.1% = 24/42). Therefore, by use of VDE technology, the sensitivity and specificity of our CADe scheme for detection of nodules, especially subtle nodules, in CXRs were improved substantially.

Index Terms—Chest radiography (CXR), computer-aided diagnosis (CAD), lung cancer, rib suppression, virtual dual energy (VDE).

Manuscript received July 24, 2012; revised September 16, 2012; accepted October 22, 2012. Date of publication November 15, 2012; date of current version January 16, 2013. This work was supported in part by the National Science Foundation of China under Grant 81101116, the National Institutes of Health under Grant S10RR021039 and Grant P30CA14599, and the Jiangsu Province Key Technology R&D Program BE2012630. Asterisk indicates corresponding author.

*S. Chen is with the University of Shanghai for Science and Technology, Shanghai 200093, China (e-mail: chnshn@hotmail.com).

K. Suzuki is with the Department of Radiology, University of Chicago, Chicago, IL 60601 USA (e-mail: suzuki@ucchicago.edu).

Color versions of one or more of the figures in this paper are available online at <http://ieeexplore.ieee.org>.

Digital Object Identifier 10.1109/TBME.2012.2226583

I. INTRODUCTION

CURRENTLY, the overall five-year survival rate for lung cancer patients is only 14% [1]. Early detection and treatment of lung cancers can improve the survival rate by 50% if the tumor is detected early at Stage 1, which is a solitary and circumscribed lung nodule.

For detection of lung cancer at an early stage, computed tomography (CT) is a more sensitive imaging modality [2]. However, chest radiographs (CXR) are used far more commonly for chest diseases because they are the most cost-effective, routinely available, and dose-effective diagnostic tool [3], [4]. Because CXRs are so widely used, improvements in the detection of lung nodules in CXRs could have a significant impact on early detection of lung cancer. Studies have shown that, however, 30% of nodules in CXRs were missed by radiologists in which nodules were visible in retrospect, and that 82–95% of the missed nodules were partly obscured by overlying bones such as ribs and clavicles [5], [6]. Such nodules would be more conspicuous on the soft-tissue images obtained by using the dual-energy subtraction technique [7].

Therefore, a computer-aided detection (CADe) scheme [8], [9] for nodules in CXRs has been investigated for assisting radiologists in improving their sensitivity. Although a great deal of work has been done by researchers to improve the performance of CADe schemes, CADe schemes still produce a relatively large number of false positives (FPs). This would distract radiologists in their detection and reduce radiologists’ efficiency. In addition, radiologists may lose their confidence with the CADe scheme as a useful tool. Matsumoto *et al.* conducted observer studies [10], which showed that, if a CADe scheme had a high FP rate of 11 per image, radiologists’ accuracy in detecting nodules was not improved when they were aided by computer output, even though the scheme had a high sensitivity of 80%. Radiologists’ accuracy, however, was significantly improved if the CADe scheme had a simulated low FP rate with the same sensitivity. Therefore, having a low FP rate is critical for a CADe scheme to be useful. A number of investigators developed FP reduction methods [11]–[13]. Yoshida *et al.* proposed a method called local contralateral subtraction to remove normal anatomic structures in CXRs based on the symmetry between the left and right lung regions for FP reduction [11]. Suzuki *et al.* developed a multiple massive-training artificial neural networks (MTANNs) to reduce the number of FPs produced by their CADe scheme [12]. Loog *et al.* investigate if the conspicuity of lung nodules increases when applying the suppression technique in CXR. Other abnormalities may also be detected, classified, and quantified more accurately if the bony anatomy is adequately suppressed [14].

A major challenge for current CADE schemes is to detect the nodules overlapping ribs, rib crossings, and clavicles, because a majority of FPs is caused by these structures [15], [16]. This leads to lowering the sensitivity as well. To detect such nodules overlapping ribs and clavicles, Kido *et al.* developed a CADE scheme based on single-exposure dual-energy computed radiography [17], [18]. A dual-energy subtraction technique [19], [20] is a technique for separating soft tissue from bones in CXRs by use of two X-ray exposures at two different energy levels. In spite of its great advantages, a limited number of hospitals use a dual-energy radiography system, because specialized equipment is required, and the radiation dose can be double. To address the issue of the availability of dual-energy systems, Suzuki *et al.* developed an image-processing technique called virtual dual-energy (VDE) radiography for suppressing ribs and clavicles in CXRs by means of a multiresolution MTANN [21], [22]. The real dual-energy images were used as the teaching images for training of the multiresolution MTANN. Once trained, real dual-energy images were not necessary any more. The trained MTANN suppressed ribs and clavicles in standard CXRs substantially, while the visibility of nodules and lung vessels was maintained.

In this study, we developed a CADE scheme for detection of pulmonary nodules by use of the MTANN VDE technology to improve the sensitivity for nodules overlapping ribs and clavicles and to reduce FPs caused by these structures.

II. MATERIALS AND METHOD

A. Database of CXRs

To train our CADE scheme, we collected 300 cases with nodules and 100 normal cases from six medical institutions by use of screen-film systems, computed radiography systems, and digital radiography systems. All nodules were confirmed by CT, and the locations of the nodules were confirmed by one of the chest radiologists. The nodule size ranged from 5 to 40 mm.

To facilitate comparisons of our VDE-based CADE scheme with our original scheme [23] and future comparisons with other methods, we used the JSRT database [24], which is publicly available. The posteroanterior CXRs in the database were collected from 14 medical institutions by use of screen-film systems over a period of three years. All nodules in the CXRs were confirmed by CT, and the locations of the nodules were confirmed by three chest radiologists. The images were digitized to yield 12-bit CXRs with a resolution of 2048×2048 pixels. The size of a pixel was 0.175×0.175 mm. The original database contained 93 normal cases and 154 cases with confirmed lung nodules. The nodules were grouped into five categories, based on the degree of subtlety for detection.

We created a database for evaluating our VDE-based CADE scheme by excluding from the full JSRT database the nodules in the opaque portions of the CXR that correspond to the retrocardiac and subdiaphragmatic regions of the lung, because the purpose of using our CADE scheme was to detect nodules in the lung fields [23]. As a result, 140 nodule cases and 93 normal cases were selected and included in the database (i.e., a subset of the JSRT database) for our experiments. Note that evaluations

of CADE schemes in past studies [25], [26] were performed without nodules in the opaque portions of CXRs for the same reason. Chen *et al.* [23] gave the characteristics of the nodules in our testing database.

B. Original Computerized Scheme for Nodule Detection

Our original CADE scheme for detection of lung nodules in CXRs consisted of four major steps: 1) segmentation of lung fields based on our multisegment active shape model (M-ASM); 2) two-stage nodule enhancement and nodule candidate detection; 3) segmentation of nodule candidates by use of our clustering watershed algorithm; and 4) feature analysis and classification of the nodule candidates into nodules or non-nodules by use of a nonlinear support vector machine (SVM) classifier [23].

To summarize, our M-ASM for lung segmenting is an improved model of the Coates *et al.* formulation [27] by fixating selected nodes at specific structural boundaries called transitional landmarks. The transitional landmarks determined multiple segments, each of which corresponded to a specific boundary type such as the heart, aorta, and rib-cage. The node-specified ASM was built using a fixed set of equally spaced feature nodes for each boundary segment. This allowed the nodes to learn local appearance models for a specific boundary type, rather than generalizing over multiple boundary types, which resulted in a marked improvement in boundary accuracy.

After the lungs were segmented, a background-trend-correction technique based on the following second-order bivariate polynomial function was applied to the segmented lung field: $F(x, y) = ax^2 + by^2 + cxy + dx + ey + f$ where $a, b, c, d, e,$ and f are coefficients. Then, our two-stage nodule enhancement technique produced a nodule-enhanced image and a nodule-likelihood map. The first stage of the technique enhanced nodules by use of two different types of gray-level morphologic opening operators [28]: one enhanced nodules; the other suppressed ribs. The second stage of our nodule enhancement converted the nodule-enhanced image into a nodule likelihood map by use of a directional gradient magnitude filter. Local peaks in the map were detected as nodule candidates.

To segment the nodule candidates, our “coarse-to-fine” segmentation technique based on morphologic filtering and improved watershed segmentation was employed. We applied a binary morphologic erosion operator to the nodule candidate regions to break connections between the nodule and non-nodule regions. Next, a binary morphologic dilation operator dilated the connected region. As a result, a single connected region representing a rough nodule candidate was obtained. To refine the rough segmentation, we developed a clustering watershed segmentation technique. Peaks within the rough nodule candidate region in the nodule-enhanced image were obtained and used for initializing the watershed segmentation algorithm [29]. With the watershed segmentation, the rough nodule candidate region was divided into several catchment basins. Each minimum point was surrounded by a catchment basin associated with it; thus, there were one or more peaks, each of which was surrounded by a cluster of connected pixels that constituted a catchment basin. From the multiple catchment basins, a single

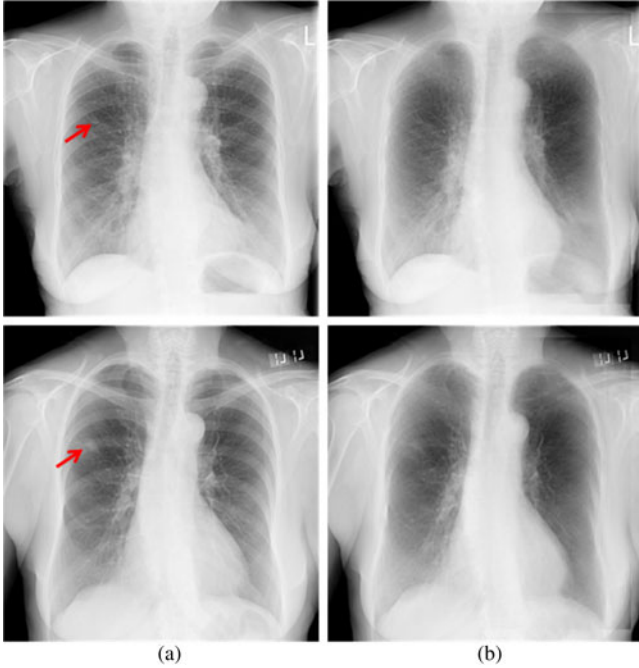


Fig. 1. Examples of VDE images in which ribs and clavicles were suppressed by using our MTANN technique. (a) Original CXR. (b) VDE soft-tissue image. Arrows indicate nodules.

nodule candidate region was determined by use of the following clustering method: first, a primary cluster was defined as a cluster that contained the nodule candidate location (as a point) determined by the initial nodule candidate detection step. Next, clusters connected to the primary cluster were added. The connected clusters were identified by use of the criterion that the minimum value between the peak in the primary cluster and each of the other peaks was larger than a threshold value.

Finally, 31 shape, gray-level, texture, and specific FP features were extracted from nodule candidates. A nonlinear SVM with a Gaussian kernel was employed for classification of the nodule candidates. We selected this classifier because its generalization ability is relatively high with a small number of training samples.

The SVM classifier was trained/tested with a leave-one-out cross-validation test. The performance of the SVM classifier was evaluated by use of free-response receiver operating characteristic (FROC) analysis [30].

C. Creation of VDE Images

An image-processing technique for suppression of ribs and clavicles in CXRs has been developed by means of a multiresolution MTANN [21], [31]. With this technique, ribs and clavicles in CXRs can be suppressed substantially, while soft tissues such as lung nodules and vessels are maintained. Fig. 1 shows examples of VDE images in which ribs and clavicles were suppressed by use of the MTANN technique. MTANN is a highly nonlinear filter that can be trained by use of input CXRs and the corresponding "teaching" images. Bone images obtained by use of a dual-energy radiography system were used as the teaching images.

The MTANN consisted of a linear-output ANN regression model that is capable of operating on image data directly [32]. Input CXRs are divided pixel by pixel into a large number of overlapping subregions. Single pixels corresponding to the centers of the input subregions are extracted from the teaching images as teaching values, represented by

$$f(x, y) = NN(\vec{I}_{x,y}) \quad (1)$$

where $\vec{I}_{x,y} = \{g(x-i, y-j) | i, j \in R_s\}$ is the input vector to the MTANN which is a subregion extracted from CXR, and $f(x, y)$ is an estimate for a teaching value.

The MTANN is massively trained by using each of a large number of the input subregions together with each of the corresponding teaching single pixels. The training set of pairs of a subregion and a teaching pixel is represented by

$$\begin{aligned} & \left\{ \vec{I}(x, y), T(x, y) | x, y \in R_T \right\} \\ & = \left\{ (\vec{I}_1, T_1), (\vec{I}_2, T_2), \dots, (\vec{I}_{N_T}, T_{N_T}) \right\} \end{aligned} \quad (2)$$

where $T(x, y)$ is a teaching image, R_T is a training region which corresponds to the collection of the centers of subregion, and N_T is the number of pixels in R_T .

For a single MTANN, suppression of ribs containing various frequencies was difficult, because of the capability of a single MTANN was limited. To overcome this issue, multiresolution decomposition/composition techniques were employed. First, a lower resolution image $g_L(x, y)$ was obtained from an original higher resolution image $g_H(x, y)$ by performing downsampling with averaging, i.e., four pixels in the original image are replaced by a pixel having the mean value for the four pixel values, represented by

$$g_L(x, y) = \frac{1}{4} \sum_{i,j \in R_{22}} g_H(2x-i, 2y-j) \quad (3)$$

where R_{22} is a 2×2 pixel region. The lower resolution image is enlarged by upsampling with pixel substitution, i.e., a pixel in the lower resolution image is replaced by four pixels with the same pixel value, as follows:

$$g_L^U(x, y) = g_L(x/2, y/2). \quad (4)$$

Then, a higher resolution difference image $d_H(x, y)$ is obtained by subtraction of the enlarged lower resolution image from the higher resolution image, represented by

$$d_H(x, y) = g_H(x, y) - g_L^U(x, y). \quad (5)$$

These procedures are performed repeatedly, producing further lower resolution images. Thus, multiresolution images having various frequencies are obtained by use of the multiresolution decomposition technique.

An important property of this technique is that exactly the same original-resolution image $g_H(x, y)$ can be obtained from

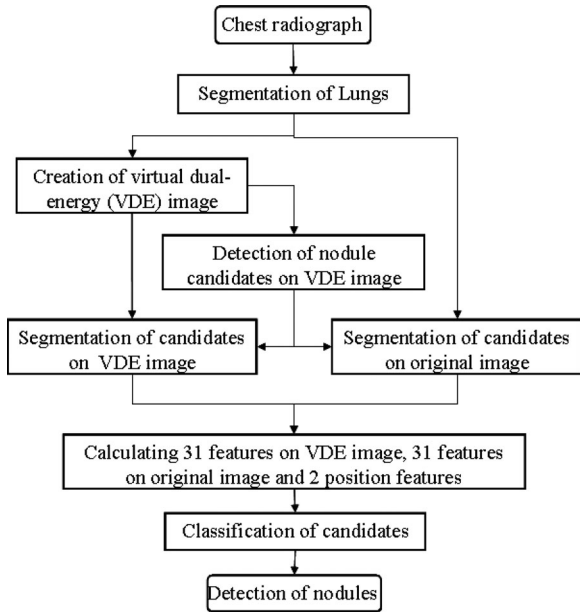


Fig. 2. Main diagram for our CADe scheme with the VDE technology based on MTANNs.

the multiresolution images, as follows:

$$g_H(x, y) = g_L^U(x, y) + d_H(x, y). \quad (6)$$

Therefore, we can process multiresolution images independently instead of processing original high-resolution images directly, i.e., with these techniques, the processed original high-resolution image can be obtained by composing of the processed multiresolution images.

After training with input CXRs and the corresponding dual-energy bone images, the multiresolution MTANN is able to produce bone images that are expected to be similar to the teaching bone images. For suppression of ribs and clavicles in an original CXR $g(x, y)$, a VDE bone image $f_b(x, y)$ produced by the trained multiresolution MTANN is subtracted from the original CXR with the lung masking image $m(x, y)$ as follows:

$$f_s(x, y) = g(x, y) - w_c \times f_b(x, y) \times m(x, y) \quad (7)$$

where w_c is a weighting parameter for determining the contrast of ribs. By changing the weighting parameter w_c , we can obtain VDE soft-tissue images with different contrasts of ribs.

D. CAD Scheme Combined With VDE Technique

Fig. 2 shows the main diagram of our proposed CADe scheme combined with the VDE technology for detection of lung nodules in CXRs. To reduce rib-induced FPs and detect nodules overlapping ribs and clavicles, we incorporated the VDE technology in our CADe scheme. The VDE-based CADe scheme detected nodule candidates on VDE images by use of the two-stage nodule enhancement technique that was applied in our original CADe scheme. A watershed segmentation algorithm was employed to segment each candidate in both original and VDE CXRs. Sixty morphologic and gray-level-based features were extracted from each candidate from both original and VDE

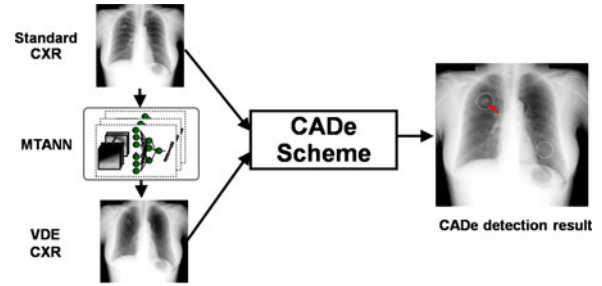


Fig. 3. Our CADe scheme for detection of lung nodules in CXRS by use of our VDE technology based on MTANNs.

CXRs which were smaller than the number of nodules in the training database. A nonlinear SVM was employed for classification of the nodule candidates into nodules or non-nodules. In our CADe scheme, only CXR acquired with a standard radiography system was inputted into our system and no specialized equipment for generating VDE image, but only software, is required (shown in Fig. 3).

Major challenges for our original CADe scheme were to detect the nodules overlapped with ribs, rib crossings, and clavicles, and reduce the FPs caused by these structures. Because of the rib and clavicle suppression in VDE images, nodules were more obvious than those in the original images. We detected nodule candidates in VDE images to improve the sensitivity for detection of nodule candidates. On the other hand, most of false nodule candidates were located in the rib crossing, clavicle regions in our original CAD scheme. We look forward to reduce most of the FPs that were caused by these structures by the incorporation of VDE image in the nodule candidate detection step.

Some nodules had similar characteristics to those of bones in terms of the shape, the size, the contrast, and the orientation. The features of these nodules may be suppressed in VDE image. Detected nodules in the nodule candidate detection step may be misclassified as non-nodules based on the features in the original image or VDE image alone. To improve the classification performance, we also extracted the same feature set at the corresponding locations of the detected nodule candidates in the corresponding original image (two coordinate features were excluded). Nodule candidate segmentation was repeated both in original and VDE images. Because of the bone suppression, the segmented contour of nodule candidate overlapped with ribs and clavicles may be more precise than that from original CXR and the feature based on the segmentation results may be more effective.

III. RESULTS

In this section, we present some experimental results to demonstrate the performance of the VDE-based CADe scheme, which incorporated the VDE technique. We first defined how to train the MTANN to create the VDE images for the CADe scheme. Next, the sensitivity for nodules candidate detection on VDE images with different rib contrast was presented and compared to that on the original image. Then, we presented the

TABLE I
FEATURES SELECTED FOR THREE CADE SCHEMES BASED ON THE ORIGINAL CXRS, VDE CXRS, AND ORIGINAL AND VDE CXRS BY USE OF THE FEATURE SELECTION METHOD

Extracted features	Original CXRs	VDE CXRs	VDE and original CXRs
Can.x	*	#	#
Can.y	*		#
Can.Grad ₁			
Can.Cv ₁	*	#	
Can.Grad ₂			
Can.Cv ₂		#	*,#
Shape ₁		#	*
Shape ₂			#
Shape ₃			
Shape ₄	*		*
Gray ₁			*
Gray ₂			
Gray ₃		#	
Gray ₄	*		
Gray ₅	*		#
Gray ₆			*
Gray ₇			
Gray ₈	*	#	
Grad ₁	*	#	
Grad ₂	*		
Grad ₃	*	#	*,#
Surface ₁		#	*
Surface ₂	*		
Surface ₃		#	
Texture ₁		#	
Texture ₂			
Texture ₃			
Texture ₄			
Texture ₅			
Texture ₆			
FP			#

* features selected from those on an original image.

features selected from those on a VDE image.

performance of the CADE scheme, which only used the VDE image to replace the original CXR for candidate detection, feature extraction, and classification. A comparison to our original scheme was also conducted. At last, the performance of the VDE-based CADE scheme was presented and compared with that of the original CADE scheme.

The overall system performance was quantified using FROC curves. The SVM classifier and linear discrimination analysis (LDA) classifier were trained/tested with a leave-one-out cross-validation test. Features for the LDA were selected by use of the stepwise feature selection method. With the selection method, we determined a single set of features from M runs of a leave-one-out cross-validation test (M is the number of features). Each feature was selected at each run after we accumulated all N results from the run (N is the number of samples). In our CADE schemes, all features extracted and selected for each CADE scheme were given in Table I. From the table, we can see that the number of selected features for VDE image was equal to that for original image. However, there were some different features selected and more density-based features instead of nodule-rib image-based features were selected for VDE image. For the VDE-based CADE scheme, 14 features were selected. It was significantly smaller than the number of true training samples.

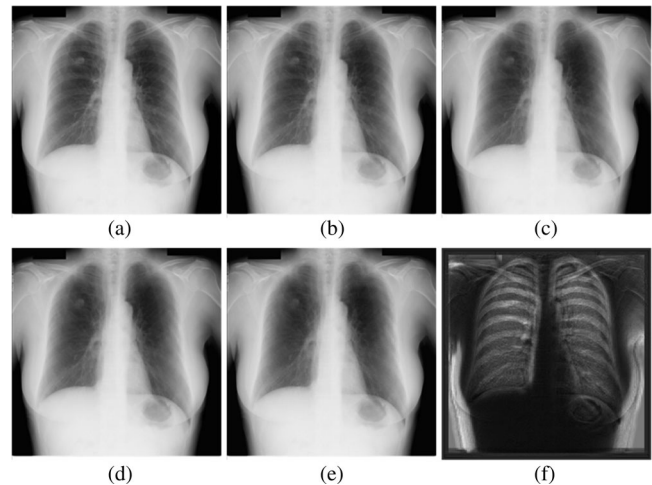


Fig. 4. Illustration of changes in rib contrast in VDE soft-tissue images and the VDE bone image used to create those soft-tissue images. (a) Original image. (b) VDE soft-tissue image with 20% rib contrast. (c) 40% rib contrast. (d) 70% rib contrast. (e) 90% rib contrast. (f) VDE bone image.

A. MTANN Training

We used four CXRs and their corresponding dual-energy bone images in a training set for training the multiresolution MTANN. One of the advantages of the MTANN technique is that it only needs a few number of dual-energy training images. In the four cases, one was a normal case and the other three contained with nodules. The training samples for the nodules were extracted by manual in order to make it cover the nodule. The size of the subregion for MTANNs was 9×9 pixels. It was sufficient to cover the width of rib in the resolution image. Three-layered MTANNs were used in our experiments where the numbers of input, hidden, and output units were 81, 20, and 1, respectively. Fig. 4 shows the VDE bone image and the VDE soft tissue images with difference rib contrast processed by multiresolution MTANN technique.

B. Nodule Candidate Detection

In this section, some experiments for nodule candidate detection based on VDE images were conducted. The “region” criterion was adopted to determine a true positive (TP) which was also applied in our original CADE scheme [23].

From Section II, we have known that the “bone-like-image” was subtracted from the original CXR to get the VDE soft tissue image. There was a parameter m_c to adjust the rib contrast in VDE image. Different parameters would have an influence on the nodule candidate detection performance. Fig. 5 shows the performance of the nodule candidate detection stage with different rib contrast in VDE image for JSRT database. The sensitivity was highest when the rib contrast parameter m_c was set 0.4. The most nodules were detected in the nodule candidate detection step and the contrast of nodule was more obvious for our CADE scheme.

In our experiments, 70 candidates that had max code values in the nodule likelihood map were selected for each image. If the distance between any two peaks was less than 5 mm, then

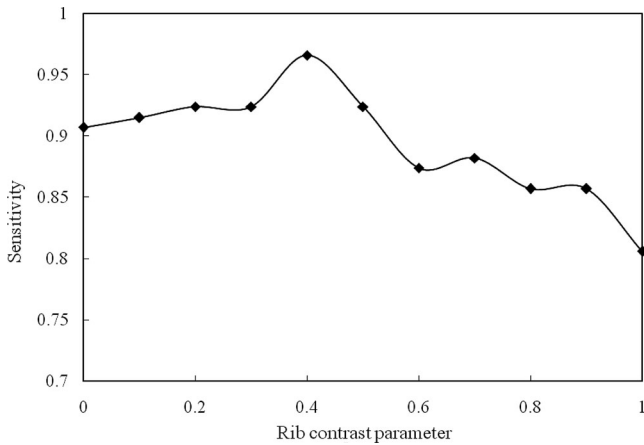


Fig. 5. Effect of the change in rib contrast on the sensitivity of our CADE scheme.

a candidate was created only from the peak with the highest value. The nodule candidate detection stage in our VDE-based CADE scheme achieved a sensitivity of 96.4% (135/140) with 70 candidates per image (a sensitivity of 92.1% (129/140) in original CADE scheme). Fig. 6(a) illustrates missed nodules in the candidate detection step from original CXR, but detected from VDE image [shown in Fig. 6(b)].

C. Performance of the Scheme Only Using VDE Image

In this experiment, VDE image was applied to replace the original image in our original CADE scheme. The nodule candidates were detected from the VDE image by use of the two-stage nodule enhancement method. Then, 31 features were extracted from the VDE image after nodule candidate segmentation. The performance of the CADE scheme only using VDE image was higher than that of original CADE scheme, i.e., it achieved a sensitivity of 65.7% (92/140) by use of VDE image and a sensitivity of 60.7% (85/140) by use of original image at an FP rate of 1.5 FPs per image for nodule cases in the JSRT database. The CADE scheme only using VDE image detected 12 more nodules, which were missed by the CADE scheme using original image at 5 FPs per image on average. Most of these nodules were very subtle or extremely subtle nodules in the JSRT database. However, five nodules were missed by the CADE scheme using VDE image, while they were detected by the original CADE scheme and they were nonsubtle nodules. So there was only 5% improvement with 5 FPs per image. It is interesting to note that the sensitivity of CADE scheme only using original image was higher than that of CADE scheme only using VDE image at a lower FP rate. With increasing the rate of FPs, the scheme using VDE image detected more subtle nodules than the original scheme. The reason is that the contrast of some nodules in VDE images was improved because of the rib suppression and it was visible for our CADE scheme to detect them. But some nodules were smoothed when using the MTANN technique to suppress the ribs in CXR. Based on this phenomenon, we also segmented the candidates and extracted the features from the original image at the same location which were detected in the

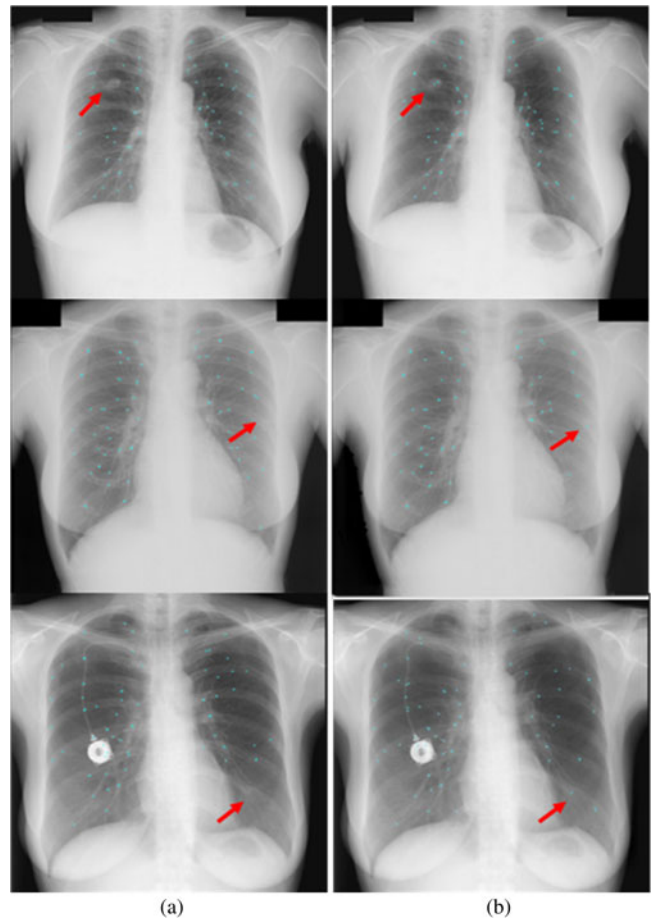


Fig. 6. Improvement in detection of nodule candidates by use of our VDE technology. (a) Nodule candidate detection results based on original images. (b) Nodule candidate detection results based on VDE images. Arrows indicate nodules. The nodules overlapping ribs that had been missed with the original images were detected with the VDE images.

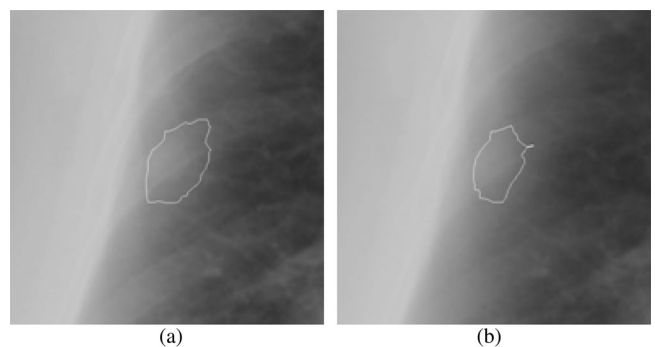


Fig. 7. Illustration of the nodules detected in the nodule candidate detection step: classified as FP by use of the features based on original image, but classified as TP by use of the features based on both the original and VDE images. (a) Nodules with segmentation results in original image. (b) Nodules with segmentation results in VDE images.

VDE image. Fig. 7 illustrates that the nodule detected in the nodule candidate detection step was classified as FP by use of the features based on original image because some rib edges were segmented as the nodule boundaries, but classified as TP by use of the features based on both original and VDE image.

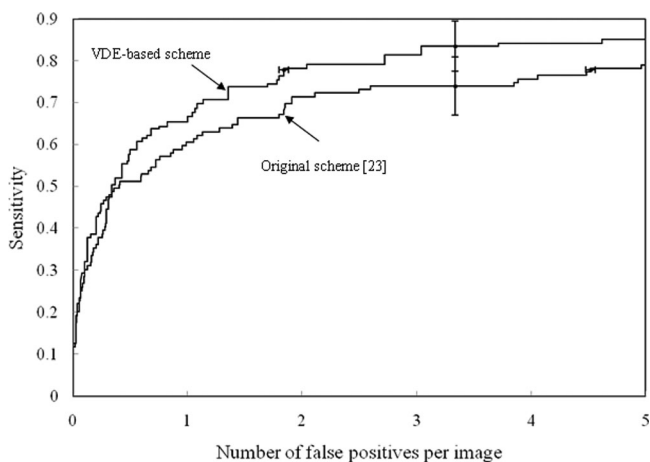


Fig. 8. FROC curves indicating the improvement in the performance of our CAde schemes with SVM classifier by use of our VDE technology for the JSRT database. Error bars indicate 95% confidence intervals.

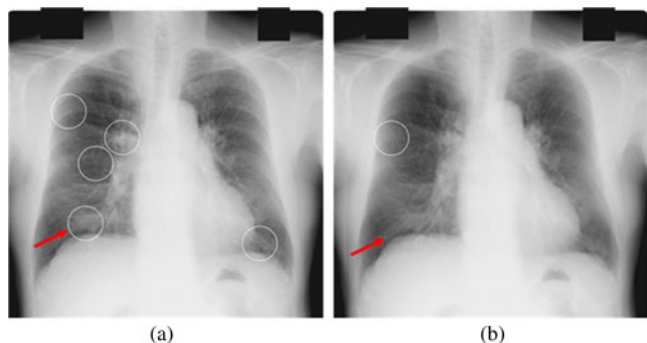


Fig. 9. Illustration of detection of nodules by our VDE-based CAde scheme (indicated by circles). (a) TP (arrow) and FPs of the original CAde scheme. (b) False negative (arrow) and FP of the VDE-based CAde scheme.

D. Performance of Scheme Using VDE Combined With Original Image

FROC curves showing the overall performances of our VDE-based CAde scheme, which combined VDE image with original image, and the original CAde scheme for the JSRT database in a leave-one-out cross-validation test with SVM are shown in Fig. 8. The performance of the VDE-based CAde scheme was substantially higher than that of the original CAde scheme, i.e., the VDE-based CAde scheme achieved a sensitivity of 85.0% (119/140) and the original CAde scheme achieved a sensitivity of 78.5% (110/140) at an FP rate of 5.0 FPs per image for the JSRT database. In the VDE-based CAde scheme, 11 nodules were detected while they were missed in the original CAD scheme and only two nodules (shown in Fig. 9) were missed.

We analyzed the CAde scheme performance according to nodule subtlety, size, and pathology, as shown in Figs. 10–12 for the JSRT database. The sensitivity was calculated in each category (i.e., the sensitivity was 100% if all nodules in a particular category were marked). Our VDE-based CAde scheme marked 66.7% (28/42) of very subtle and extremely subtle nodules with 5 FPs per image. All obvious nodules were marked with 2.5 FPs per image, and 92.1% (35/38) of relatively obvious

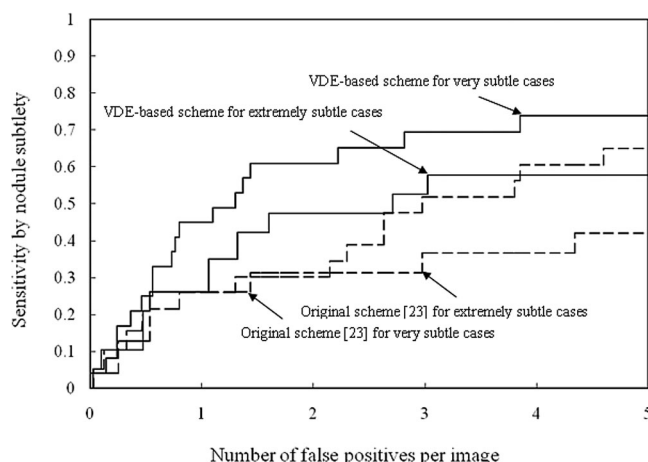


Fig. 10. FROC curves indicating the performance of the VDE-based CAde scheme by nodule subtlety for the JSRT database.

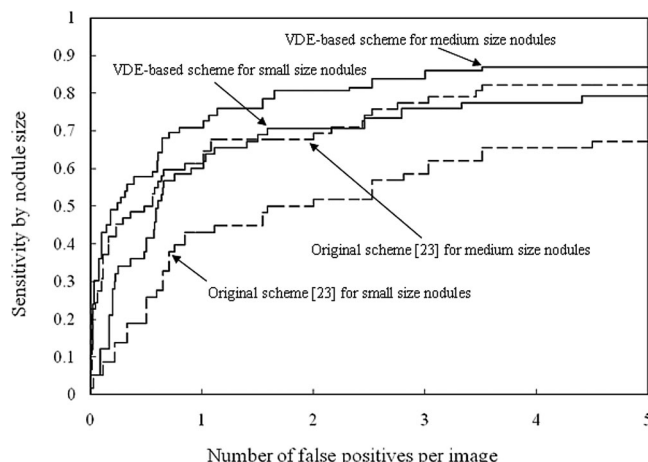


Fig. 11. FROC curves indicating the performance of the VDE-based CAde scheme by nodule size for the JSRT database.

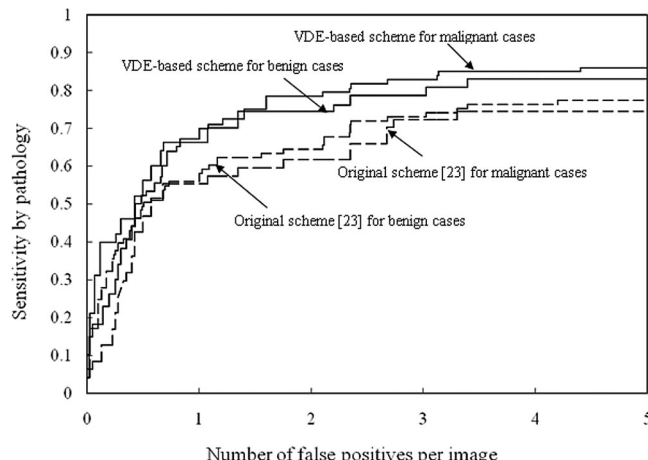


Fig. 12. FROC curves indicating the performance of the VDE-based CAde scheme by pathology for the JSRT database.

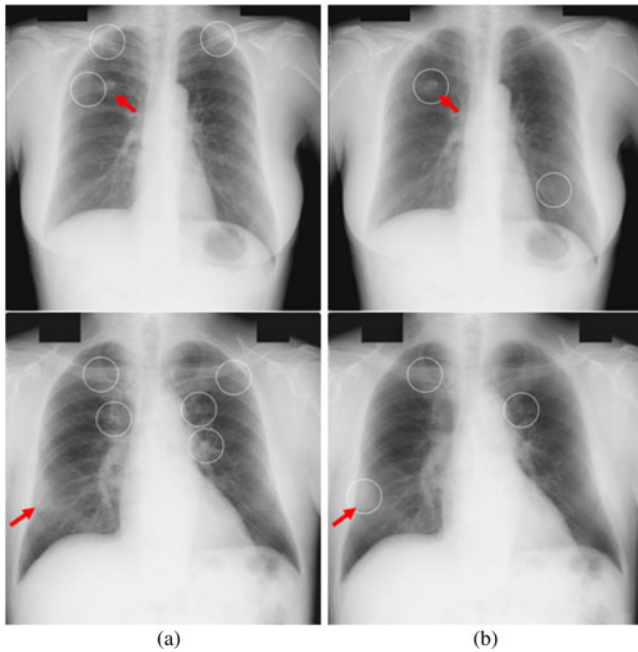


Fig. 13. Illustration of the improvement in nodule detection with our VDE technology. CADe marks are indicated by circles. (a) False negatives (arrow) and FPs of the original CADe scheme. (b) TPs (arrow) and FPs of the VDE-based CADe scheme with the VDE technology.

nodules were detected with 1.6 FPs per image. It is interesting to note that the detection result for very subtle nodules was significantly improved. This may be partially attributable to the fact that the very subtle nodules were overlapped with ribs, while in the VDE image, it was more visible to be detected. Our VDE-based CADe scheme has a high performance (a sensitivity of 87.1% (54/62) with 5.0 FPs per image) for the medium-sized nodules and a relatively high performance (a sensitivity of 79.3% (46/58) with 5.0 FPs per image) for small nodules, as shown in Fig. 11. The sensitivities for malignant and benign nodules were comparable, as shown in Fig. 12.

Several typical examples of our CADe detection results at operating points with an FP rate of 4.5 FPs per image for the JSRT database are shown in Fig. 13. The VDE-based CADe scheme detected the truth nodules with few FPs, whereas the original CADe scheme missed the truth nodules, and most of the FPs were located in the ribs, rib intersections, and the clavicles. Fig. 14 shows two examples that the FPs which were detected in the original scheme were reduced in the VDE-based CADe scheme. The VDE-based CADe scheme not only can detect more nodules which were overlapped with ribs or clavicles, but also can reduce the FPs deduced by the ribs and clavicle. Thus, the overall performance was substantially improved by use of the VDE technique.

E. Performance Comparison With Others

It is difficult to make definitive comparisons with previously published CADe schemes because of different databases, different TP criteria, different evaluation procedures, different optimization parameters, and different operating points [33]. We,

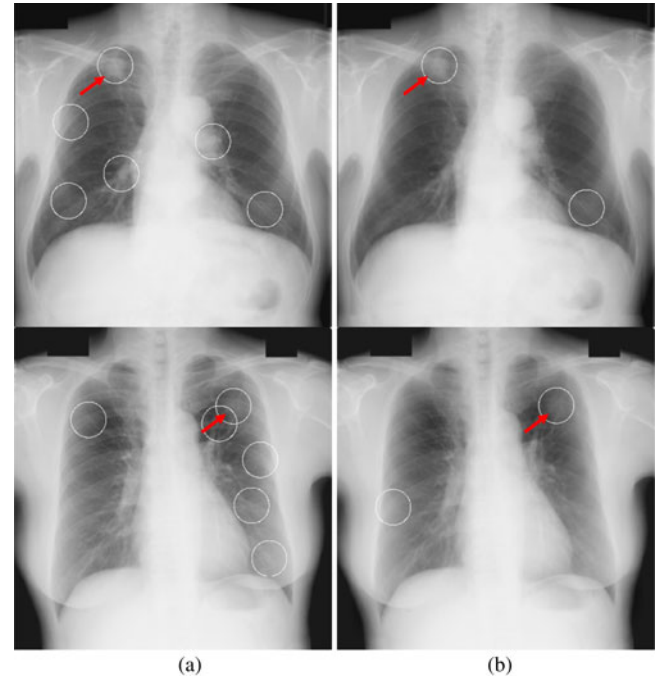


Fig. 14. Illustration of the improvement in specificity by our VDE technology. CADe marks are indicated by circles. (a) TPs (arrow) and FPs of the original CADe scheme. (b) TPs (arrow) and FPs of the VDE-based CADe scheme with the VDE technology.

TABLE II
PERFORMANCE COMPARISONS OF CADE SCHEMES THAT USED THE JSRT DATABASE FOR EVALUATION IN THE LITERATURE

	Sensitivity	FPs/image	Database
Wei et al. (2002) [34]	80% (123/154)	5.4 (1333/247)	All nodule and normal cases in JSRT (247)
Coppini et al. (2003) [35]	60% (93/154)	4.3 (662/154)	All nodules cases in JSRT (154)
Schiham et al. (2006) [13]	51% (79/154) 67% (103/154)	2.0 (308/154) 4.0 (616/154)	All nodule cases in JSRT (154)
Hardie et al. (2009) [26]	80% (112/140) 63% (88/140)	5.0 (700/140) 2.0 (280/140)	Nodule cases in JSRT (140)
Chen et al. (2011) [23]	79% (110/140) 71% (100/140)	5.0 (1165/233) 2.0 (466/233)	Nodule cases and all normal cases in JSRT (233)
VDE-based CADe	85% (119/140)	5.0 (1165/233)	Nodule cases and all normal cases in JSRT (233)

however, attempted to compare our performance with the performance reported in the literature. We found four studies in which the publicly available JSRT database was used. Table II summarizes the performance comparisons among different CADe schemes in the literature. Wei *et al.* reported that their CAD scheme achieved a sensitivity of 80% with 5.4 FPs per image for the JSRT database [34]. Hardie *et al.* reported that their scheme marked 80% of nodules in a subset of the JSRT database with 5 FPs per image [26]. Their performance was calculated by use of the “distance” criterion of 25 mm for determining TP detections. The performance of our VDE-based CADe scheme

was substantially higher than that of Hardie's CADe scheme, i.e., our VDE-based CADe scheme achieved a sensitivity of 85.0% (119/140) and 77.9% (109/140); Hardie's CADe scheme achieved a sensitivity of 80.0% and 63% at FP rates of 5.0 and 2.0 per image, respectively.

IV. DISCUSSION

A dual-energy subtraction technique has been used to address the issue of obscuring bones. Dual-energy soft-tissue images can improve the detection of focal soft-tissue opacities, such as lung nodules, that may be partly obscured by overlapping ribs or clavicles. For the computerized CADe scheme, the FPs deduced by these reasons can also be reduced. In spite of the advantages, a very limited number of hospitals use radiography systems with dual-energy subtraction, because specialized equipment for obtaining dual-energy X-ray exposures is required. It is very difficult to collect a large number of lung nodule cases from the dual-energy system for CADe scheme's training and testing. Also, the radiation dose can be greater than that for standard chest radiography in some cases. Likewise dual-energy soft-tissue images, VDE images have a potential to improve the sensitivity in detecting early cancer that is partly obscured by overlying ribs, and potential to improve the specificity by differentiating nodules from other abnormalities or normal anatomic structures because of the suppression of obscuring ribs. In this paper, we proposed a VDE-based CADe scheme for lung nodule detection by use of VDE images.

For nodule candidate detection in VDE images, we can get different performance by use of different rib contrast in the VDE images. In our paper, a fixed rib contrast parameter was selected corresponding to the highest performance in candidate detection for all nodule cases in the JSRT database. However, there are still several truth nodules missed and some of these nodules could be detected in the VDE image with other rib contrast. There is a potential improvement for the performance in the nodule candidate detection. Because the rib contrast in the original image is different from case to case for the exposure dose, the rib contrast suppression parameter should be optimized based on each case.

For the final detection result, although more very subtle nodules were detected, there were some obvious nodules missed by the VDE-based CADe scheme. The main reason was that these nodules had characteristics similar to those of ribs in terms of the shape, the size, the contrast, the orientation, the texture, and the margin. Another reason was that, in our experiment, the images were scanned from films. There were not corresponding dual-energy bone images to them. The MTANN that was used to create the VDE image was trained by four cases (one was a normal case and the three contained with nodules), which were obtained from a dual-energy CR system. The rib contrast and resolution in the digital radiograph are higher than that scanned from films. When we used this trained MTANN to suppress the ribs and clavicles in CXR from JSRT, the results were not optimization. If we test our VDE-based CADe scheme on such a database that is composed of CR images, it may have a better performance. Currently, in order to address this issue

that some nodules were suppressed in VDE images, the CADe scheme incorporated VDE image with original image together and extracted the same set of features from the original image as from the VDE image. The results demonstrated that it could improve the performance effectively. For the VDE-based CADe scheme, most of the FPs were located in the hilar vessels and the diaphragm area.

We used the publicly available JSRT database to evaluate our CADe scheme. The observer studies indicated that radiologists found it particularly difficult to detect the very and extremely subtle nodules in the JSRT database and the radiologist detected only 44% of the hard cases. With an average 4 FPs per image, our VDE-based scheme correctly marked 66.7% of the hard cases. There was 10% improvement than our original scheme, and it also had a higher performance than that proposed by Schilham *et al.*, which is 41% [13]. This was a very encouraging result that our method could provide a useful clinical tool. The improved CADe scheme incorporating VDE image had a special characteristic for detecting the hard subtle nodules.

The time for processing one case with our VDE-based CADe scheme was about 115 s (including 25 s for nodule candidate detection and 90 s for candidate segmentation, features extraction, and classification in both original CXR and VDE images) on a PC-based workstation (Intel Pentium 2.4-GHz processor with a 3-GB memory). The candidate segmentation consumed most of the entire processing time. A radiologist can reference to the CADe scheme's results to take a second reading for CXR after 120 s of first reading. It can satisfy the clinical requirement.

V. CONCLUSION

We developed an advanced computerized scheme for detection of lung nodules by incorporating VDE image in which ribs and clavicles were suppressed by an MTANN technique. The performance of the CADe scheme (85% sensitivity with 5 FPs/image) provided a substantial improvement against the original CADe scheme (78% sensitivity with 5 FPs/image).

REFERENCES

- [1] American Cancer Society, *American Cancer Society Complete Guide to Complementary & Alternative Cancer Therapies*, 2nd ed. Atlanta, GA.: American Cancer Society, 2009.
- [2] C. I. Henschke, D. I. McCauley, D. F. Yankelevitz, D. P. Naidich, G. McGuinness, O. S. Miettinen, D. M. Libby, M. W. Pasmantier, J. Koizumi, N. K. Altorki, and J. P. Smith, "Early lung cancer action project: Overall design and findings from baseline screening," *Lancet*, vol. 354, pp. 99–105, Jul. 10, 1999.
- [3] G. P. Murphy, W. Lawrence, R. E. Lenhard, and American Cancer Society, *American Cancer Society Textbook of Clinical Oncology*, 2nd ed. Atlanta, GA.: American Cancer Society, 1995.
- [4] H. Zhao, S. C. Lo, M. Freedman, and Y. Wang, "Enhanced lung cancer detection in temporal subtraction chest radiography using directional edge filtering techniques," presented at the Proc. SPIE Med. Imag.: Image Process., San Diego, CA, 2002.
- [5] J. H. Austin, B. M. Romney, and L. S. Goldsmith, "Missed bronchogenic carcinoma: Radiographic findings in 27 patients with a potentially resectable lesion evident in retrospect," *Radiology*, vol. 182, pp. 115–122, Jan. 1992.
- [6] P. K. Shah, J. H. Austin, C. S. White, P. Patel, L. B. Haramati, G. D. Pearson, M. C. Shiau, and Y. M. Berkmen, "Missed non-small cell lung cancer: Radiographic findings of potentially resectable lesions evident only in retrospect," *Radiology*, vol. 226, pp. 235–241, Jan. 2003.

- [7] F. Li, R. Engelmann, K. Doi, and H. MacMahon, "Improved detection of small lung cancers with dual-energy subtraction chest radiography," *AJR Amer. J. Roentgenol.*, vol. 190, pp. 886–891, Apr. 2008.
- [8] M. L. Giger, K. Doi, and H. MacMahon, "Image feature analysis and computer-aided diagnosis in digital radiography. 3. Automated detection of nodules in peripheral lung fields," *Med. Phys.*, vol. 15, pp. 158–166, Mar.–Apr. 1988.
- [9] B. van Ginneken, B. M. ter Haar Romeny, and M. A. Viergever, "Computer-aided diagnosis in chest radiography: A survey," *IEEE Trans. Med. Imag.*, vol. 20, no. 12, pp. 1228–1241, Dec. 2001.
- [10] T. Matsumoto, K. Doi, A. Kano, H. Nakamura, and T. Nakanishi, "Evaluation of the potential benefit of computer-aided diagnosis (CAD) for lung cancer screenings using photofluorography: Analysis of an observer study," *Nippon Igaku Hoshasen Gakkai Zasshi*, vol. 53, pp. 1195–1207, Oct. 25, 1993.
- [11] H. Yoshida, "Local contralateral subtraction based on bilateral symmetry of lung for reduction of false positives in computerized detection of pulmonary nodules," *IEEE Trans. Biomed. Eng.*, vol. 51, no. 5, pp. 778–789, May 2004.
- [12] K. Suzuki, J. Shiraishi, H. Abe, H. MacMahon, and K. Doi, "False-positive reduction in computer-aided diagnostic scheme for detecting nodules in chest radiographs by means of massive training artificial neural network," *Acad. Radiol.*, vol. 12, pp. 191–201, Feb. 2005.
- [13] A. M. Schilham, B. van Ginneken, and M. Loog, "A computer-aided diagnosis system for detection of lung nodules in chest radiographs with an evaluation on a public database," *Med. Image Anal.*, vol. 10, pp. 247–258, Apr. 2006.
- [14] M. Loog, B. van Ginneken, and A. M. Schilham, "Filter learning: Application to suppression of bony structures from chest radiographs," *Med. Image Anal.*, vol. 10, pp. 826–840, Dec. 2006.
- [15] T. Matsumoto, H. Yoshimura, K. Doi, M. L. Giger, A. Kano, H. MacMahon, K. Abe, and S. M. Montner, "Image feature analysis of false-positive diagnoses produced by automated detection of lung nodules," *Investigative Radiol.*, vol. 27, pp. 587–597, Aug. 1992.
- [16] X. W. Xu, K. Doi, T. Kobayashi, H. MacMahon, and M. L. Giger, "Development of an improved CAD scheme for automated detection of lung nodules in digital chest images," *Med. Phys.*, vol. 24, pp. 1395–1403, Sep. 1997.
- [17] S. Kido, K. Kuriyama, C. Kuroda, H. Nakamura, W. Ito, K. Shimura, and H. Kato, "Detection of simulated pulmonary nodules by single-exposure dual-energy computed radiography of the chest: Effect of a computer-aided diagnosis system (Part 2)," *Eur. J. Radiol.*, vol. 44, pp. 205–209, Dec. 2002.
- [18] S. Kido, H. Nakamura, W. Ito, K. Shimura, and H. Kato, "Computerized detection of pulmonary nodules by single-exposure dual-energy computed radiography of the chest (part 1)," *Eur. J. Radiol.*, vol. 44, pp. 198–204, Dec. 2002.
- [19] R. Glocker and W. Frohnmayer, "Über die röntgenspektroskopische Bestimmung des Gewichtsanteiles eines Elementes in Gemengen und Verbindungen," *Annalen der Physik*, vol. 76, pp. 369–395, 1925.
- [20] B. Jacobson and R. S. Mackay, "Radiological contrast enhancing methods," *Adv. Biol. Med. Phys.*, vol. 6, pp. 201–261, 1958.
- [21] K. Suzuki, H. Abe, H. MacMahon, and K. Doi, "Image-processing technique for suppressing ribs in chest radiographs by means of massive training artificial neural network (MTANN)," *IEEE Trans. Med. Imag.*, vol. 25, no. 4, pp. 406–416, Apr. 2006.
- [22] K. Suzuki, H. Abe, F. Li, and K. Doi, "Suppression of the contrast of ribs in chest radiographs by means of massive training artificial neural network," in *Proc. SPIE Med. Imag.*, San Diego, CA, 2004, pp. 1109–1119.
- [23] S. Chen, K. Suzuki, and H. MacMahon, "Development and evaluation of a computer-aided diagnostic scheme for lung nodule detection in chest radiographs by means of two-stage nodule enhancement with support vector classification," *Med. Phys.*, vol. 38, pp. 1844–1858, 2011.
- [24] J. Shiraishi, S. Katsuragawa, J. Ikezoe, T. Matsumoto, T. Kobayashi, K. Komatsu, M. Matsui, H. Fujita, Y. Koda, and K. Doi, "Development of a digital image database for chest radiographs with and without a lung nodule: Receiver operating characteristic analysis of radiologists' detection of pulmonary nodules," *AJR Amer. J. Roentgenol.*, vol. 174, pp. 71–74, Jan. 2000.
- [25] J. Shiraishi, Q. Li, K. Suzuki, R. Engelmann, and K. Doi, "Computer-aided diagnostic scheme for the detection of lung nodules on chest radiographs: Localized search method based on anatomical classification," *Med. Phys.*, vol. 33, pp. 2642–2653, Jul. 2006.
- [26] R. C. Hardie, S. K. Rogers, T. Wilson, and A. Rogers, "Performance analysis of a new computer aided detection system for identifying lung nodules on chest radiographs," *Med. Image Anal.*, vol. 12, pp. 240–258, Jun. 2008.
- [27] T. F. Cootes, A. Hill, C. J. Taylor, and J. Haslam, "Use of active shape models for locating structures in medical images," *Image Vis. Comput.*, vol. 12, pp. 355–365, 1994.
- [28] J. Serra, *Image Analysis and Mathematical Morphology*, vol. 1. New York: Academic, 1982.
- [29] L. Vincent and P. Soille, "Watersheds in digital spaces: An efficient algorithm based on immersion simulations," *IEEE Trans. Pattern Anal. Mach. Intell.*, vol. 13, no. 6, pp. 583–598, Jun. 1991.
- [30] J. P. Egan, G. Z. Greenberg, and A. I. Schulman, "Operating characteristics, signal detectability, and the method of free response," *J. Acoust. Soc. Amer.*, vol. 33, pp. 993–1007, 1961.
- [31] K. Suzuki, H. Abe, F. Li, and K. Doi, "Suppression of the contrast of ribs in chest radiographs by means of massive training artificial neural network," in *Proc. SPIE Med. Imag.*, 2004, vol. 5370, pp. 1109–1119.
- [32] K. Suzuki, I. Horiba, and N. Sugie, "Neural edge enhancer for supervised edge enhancement from noisy images," *IEEE Trans. Pattern Anal. Mach. Intell.*, vol. 25, no. 12, pp. 1582–1596, Dec. 2003.
- [33] R. M. Nishikawa, M. L. Giger, K. Doi, C. E. Metz, F. F. Yin, C. J. Vyborny, and R. A. Schmidt, "Effect of case selection on the performance of computer-aided detection schemes," *Med. Phys.*, vol. 21, pp. 265–269, Feb. 1994.
- [34] J. Wei, Y. Hagihara, A. Shimizu, and H. Kobatake, "Optimal image feature set for detecting lung nodules on chest X-ray images," in *Proc. Comput.-Assisted Radiol. Surg.*, 2002, pp. 706–711.
- [35] G. Coppini, S. Diciotti, M. Falchini, N. Villari, and G. Valli, "Neural networks for computer-aided diagnosis: Detection of lung nodules in chest radiograms," *IEEE Trans. Inf. Technol. Biomed.*, vol. 7, no. 4, pp. 344–357, Dec. 2003.

Authors' photographs and biographies not available at the time of publication.